ADVANCED ELECTRONIC MATERIALS
www.advelectronicmat.de

Highly Crystallized Tin Dioxide Microwires toward Ultraviolet Photodetector and Humidity Sensor with High Performances

*Hui Liu, Chaolei Zuo, Ziliang Li, Xinya Liu, and Xiaosheng Fang**

The rapid development of artificial intelligent and internet of things calls for high-performance multifunctional devices for synchronous detection of a wide variety of environmental signals, such as gas, light, and humidity. Herein, highly crystallized tin dioxide (SnO_2) microwires (MWs) with low density of point defects are synthesized by the chemical vapor deposition method and constructed into a multifunctional device for photo and humidity sensing. The device shows excellent photoelectric performances, for example, ultralow dark current of ≈10^{-13} A, ultrahigh on–off ratio of >10^7, UV/visible rejection ratio of $R_{300\ nm}/R_{400\ nm} > 10^7$, specific detectivity ($D^*$) of 1.16×10^{15} Jones, linear dynamic range (LDR) of 152 dB, high responsivity of 18 A W^{-1}, and fast photoresponse speed of t_{rise}/t_{decay} = 2.7 µs/2.5 ms at 5 V bias. Furthermore, the p-CuI/n-SnO_2 heterojunction shows outstanding self-powered properties, such as responsivity of 8.98 mA W^{-1}, specific detectivity of 1.98×10^{12} Jones and LDR of 106 dB at 0 V bias. Additionally, the SnO_2 MWs also show high sensitivity to ambient humidity changes. Therefore, the SnO_2 MWs show high potential for multifunctional applications, such as UV photodetector and humidity sensor.

1. Introduction

As one of the most extensively investigated metal oxides, tin dioxide (SnO_2) is a very promising n-type semiconducting material with numerous advantages,[1–4] such as direct and wide bandgap ($E_g \approx 3.6$ eV), high exciton binding energy (≈130 meV), high carrier concentrations (≈10^{20} cm^{-3}), superior electron transport properties and high stability in harsh environmental conditions, enabling it to be an attractive material candidate for a wide range of potential applications, for example, chemical and gas sensors,[3,4] transparent conductive electrodes,[4,5] electrocatalysts,[6,7] solar cells,[8,9] lithium-ion batteries,[10,11] field emitters[12] as well as UV photodetectors (PDs).[13,14] Various preparation technologies, such as sol–gel method, solvothermal process, and chemical vapor deposition (CVD) reaction[3,4] have been used for synthesizing SnO_2 with diverse morphologies. Among them, the CVD reaction is an effect method for both top–down and bottom–up synthesis of highly crystallized materials.[15] However, there are still difficulties for realizing high-performance UV PDs based on the SnO_2 single crystals. For example, SnO_2 nanowires which display ultrahigh external quantum efficiency (EQE) have been obtained,[16] but further application of this material is limited by its slow response and high dark current. A kinked SnO_2 nanowire with improved photoresponse speed via microstructural optimization have been prepared,[17] however, its dark current is still not low enough. Besides, the complex processing technologies, such as photolithography, metal deposition, and lift-off, are needed during the fabrication of these nanowire-based devices.

It is known that the surficial defect state resulting from the large surface to volume ratio of nanomaterials is one of the most possible reasons for their slow response.[17,18] In addition, the optical and electrical properties of SnO_2 are also greatly influenced by the crystallinity and defect states, which can be modulated through the alteration of some processing factors such as temperature, gas atmosphere, raw materials, dopant element, and concentration.[18,19] Generally, the SnO_2 in its stoichiometry form is good insulator,[2,4] however, nominally undoped SnO_2 is highly conductive and transparent due to the extremely low formation energies of the intrinsic defects (i.e., tin interstitial and oxygen vacancy), which donate electrons to the conduction band without increasing optical interband absorption.[2,4] Fortunately, these disadvantages can be attenuated through rational design. For instance, an accelerated photoresponse of the SnO_2 microwires (MWs)-based UV PD can be realized by decreasing the density of point defects, and self-powered performance was achieved via a surface modification with a p-type CuZnS transparent semiconductor.[18] SnO_2 nanowires with controllable surface state for constructing high-performance UV PD with ultrahigh selectivity have been reported.[20]

With the rapid development of the artificial intelligent and internet of things, the construction of multifunctional sensors with flexible, silicon-compatible, high-performance, low energy consumption, and low cost is becoming attractive research focus in the recent years.[21–25] To achieve these goals, the construction of heterojunction is a promising alternative

H. Liu, C. L. Zuo, Z. L. Li, X. Y. Liu, X. S. Fang
Department of Materials Science
Fudan University
Shanghai 200433, P. R. China
E-mail: xshfang@fudan.edu.cn
H. Liu
Department of Chemistry
Hubei Minzu University
Enshi, Hubei 445000, P. R. China
The ORCID identification number(s) for the author(s) of this article can be found under https://doi.org/10.1002/aelm.202100706.

DOI: 10.1002/aelm.202100706

due to the formation of built-in electric field,[26–29] which can effectively facilitate the separation of photogenerated electron–hole pairs without external power source (i.e., self-power) and allows the device to work independently and sustainably in a non-energy consumption mode.[30,31] In addition, it is known that the absorption/desorption of certain gases on the oxide semiconductor surface can induce the change of the electrical resistivity.[3] Therefore, the metal oxide-based gas sensors play an important role in detecting toxic pollutants or non-toxic gases, such as CO, H_2S, NO_x, SO_2, H_2 and H_2O.[3] Since SnO_2 can convert external physical or chemical stimuli into electrical signals (e.g., UV irradiation and different chemical substances), a device with multifunction might be realized. Herein, single-crystal SnO_2 MWs with high crystallinity have been synthesized using the facile CVD method. Furthermore, a high-performance self-powered p-CuI/n-SnO_2 heterojunction-based UV PD has been achieved. Additionally, the SnO_2 MW-based device also exhibits fast response to humidity changes. The results indicate the high potential of the SnO_2 MWs for multifunctional application in UV detection and humidity sensing.

2. Result and Discussion

From the scanning electron microscope (SEM) images (**Figure 1**a) and the optical picture (Figure S1, Supporting Information), it is observed that the as-prepared SnO_2 are freestanding MWs. Statistics indicates that the width range from 10 to 40 µm, and the length are diverse from several hundred micrometers to more than one centimeter. The growth mechanism

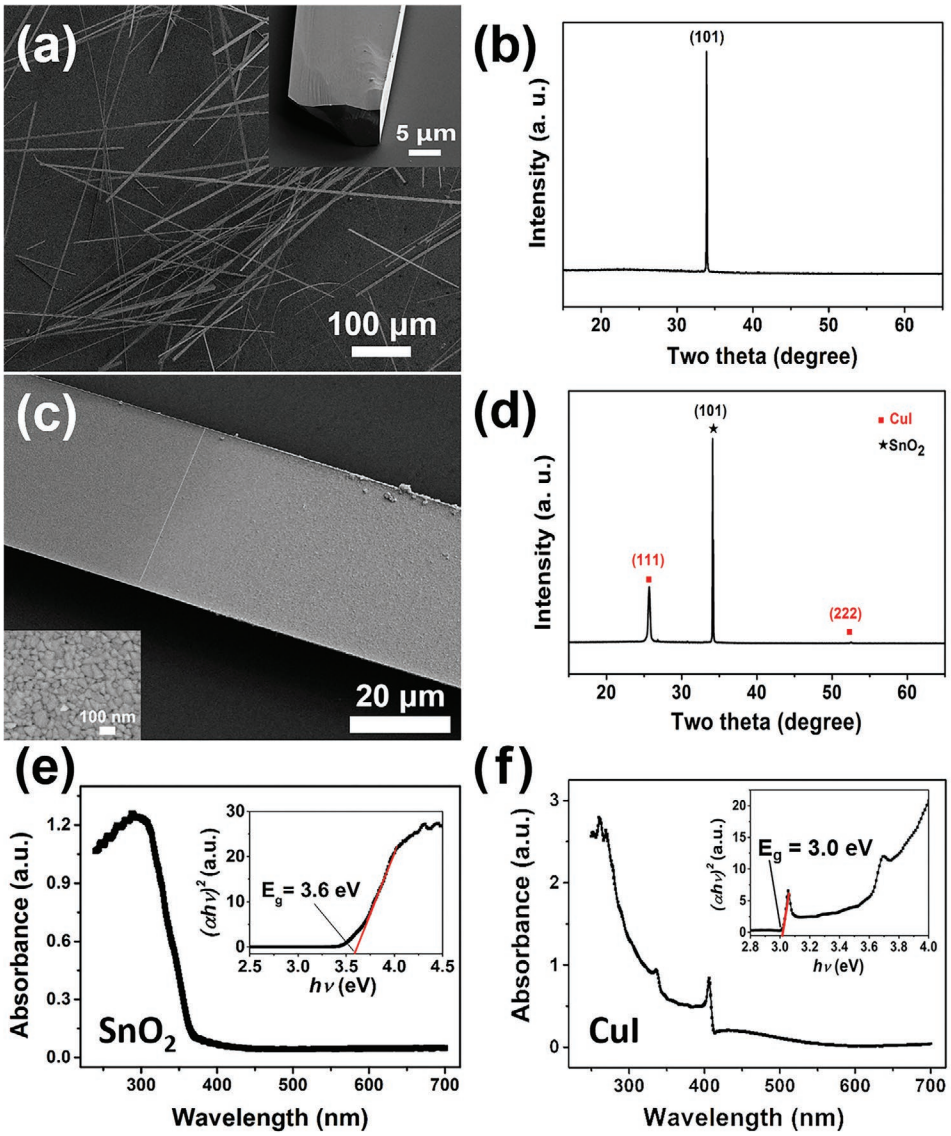

Figure 1. Basic characterizations of the pristine SnO_2 and the p-CuI/n-SnO_2 MWs. a,c) SEM images of the pristine SnO_2 MWs (inset is the enlarged cross-section image) and the p-CuI/n-SnO_2 MW (inset is the enlarged image of CuI on SnO_2). b,d) XRD patterns of a single SnO_2 MW and multiple p-CuI/n-SnO_2 MWs. e,f) UV–vis absorption spectra of the pristine SnO_2 and the CuI film. (Inset: the plot of $(\alpha h\nu)^2$ vs $h\nu$ for the SnO_2 MWs and the CuI film, where E_g is the optical bandgap)

of the SnO_2 MWs is regarded as a vapor–solid process, since no metal has been used as catalyst and no particle can be found on the tip of the SnO_2 MWs, as shown in Figure 1a. The following chemical reactions are proposed to take place during the thermal evaporation process:[19,32–36]

$$C(s) + SnO_2(s) = SnO(g) + CO(g) \quad (1)$$

$$CO(g) + SnO_2(s) = SnO(g) + CO_2(g) \quad (2)$$

$$2SnO(g) = Sn(g) + SnO_2(s) \quad (3)$$

$$Sn(g) + O_2(g) = SnO_2(s) \quad (4)$$

$$2SnO(g) + O_2(g) = 2SnO_2(s) \quad (5)$$

First, metastable SnO forms by the reaction of SnO_2 with active carbon and carbon monoxide (Equations (1) and (2)),[33,34] then the SnO decomposes into SnO_2 and Sn (Equation (3)),[19,33,34] the SnO_2 also forms in the presence of O_2 (Equations (4) and (5)).[35,36] Finally, the SnO_2 precipitates on the surface of the p-type Si substrate or the alumina boat which act as nucleation sites and initiate the growth of SnO_2 MWs via the vapor–solid mechanism.

The XRD patterns of an individual SnO_2 MW and multiple SnO_2 MWs are shown in Figure 1b and Figure S2a, Supporting Information. The diffraction peaks are identified as the tetragonal SnO_2 phase (PDF 41-1445). Noteworthy, the sharp reflection of the SnO_2 (101) in the XRD patterns and smooth surface (Figure S2a, Supporting Information, and inset of Figure 1a) indicate that the SnO_2 MWs are highly crystallized, which probably results from the oxygen atmosphere and high growth temperature and ultimately contributes to the decrease of point defects. The XPS result (Figure S2b–d, Supporting Information) indicates that only Sn and O exist in the sample. The two peaks at 486.6 and 494.9 eV are assigned to Sn 3d 5/2 and Sn 3d 3/2, respectively, indicating the existence of Sn^{4+} on the surface of the SnO_2 MWs.[16] A detectable contrast difference can be observed on the p-CuI/n-SnO_2 MW, as indicated by the dotted lines in Figure 1c and Figure S3a, Supporting Information. The CuI appears in the form of nanosheets and nanoparticles with an average size of ≈60 nm (inset of Figure 1c and Figure S3, Supporting Information). From the XRD pattern in Figure 1d, it is observed that besides the (101) peak of SnO_2, two peaks located at 25.5° and 52.3° are ascribed to the (111) and (222) diffractions of CuI (PDF 06-0246).

The optical properties are characterized by the UV–vis spectrum for a better insight into the band structure of SnO_2 MWs and CuI (Figure 1e,f). Accordingly, the SnO_2 MWs and CuI film almost show negligible absorption in the visible range and a sharp absorption edge at 350 and 415 nm, respectively. As for direct bandgap semiconductors, it is well established that the optical bandgap (E_g) and absorption coefficient (α) near the absorption edge are coupled with the following equation:[37,38]

$$(\alpha h\nu)^2 = A(h\nu - E_g) \quad (6)$$

where A is the absorption constant that relates to the effective masses associated with the valence and conduction bands, and $h\nu$ is the photon energy.[39] The bandgap of the SnO_2 MW and the CuI film are fitted to be 3.6 eV (344 nm) and 3.0 eV (413 nm), respectively (inset image of Figure 1e,f).

To investigate the photoelectric performance of the SnO_2 MWs, a SnO_2 MW-based UV PD (width ≈ 38 μm) is constructed by manually patterning two drops of Ag paste at both ends (Inset image in **Figure 2**a). In Figure 2a, it is clearly seen that the dark current is lower than 0.1 pA between −5 and 5 V, corresponding to a high resistance of ≈5×10^{14} Ω (as deduced from the dark current at 5 V) which indicates the low-density of intrinsic detects within the SnO_2 MWs.[2,4] Time-dependent photo current measurements operated at 0.01–5 V under 300 nm (1.612 mW cm^{-2}) light illumination is conducted and the result is presented in Figure 2b and Figure S4, Supporting Information. The stable and rapid photoresponse reveals the excellent stability and reliability of the PD. The calculated on/off ratios at 5 and 0.01 V bias are 3.5×10^7 and 1×10^4 under 300 nm illumination, respectively, which is the highest one among the previous reported SnO_2-based PDs (Table S1, Supporting Information). For a more precise measurement of the response speed, we have employed a system with a digital oscilloscope (Tektronix DPO5140B) and an Nd:YAG 355 nm pulsed laser system with 3–5 ns pulse duration. Figure 2c displays the transient current output to 10 Hz 355 nm laser pulse under 5 V bias, in which an ultrafast, highly stable, and repeatable photoresponse can be observed. The rise time (t_{rise}, defined as the time of current increasing from 10% to 90%) and decay time (t_{decay}, defined as the time of current decreasing from 90% to 10%) of the device are deduced to be 2.7 μs and 2.5 ms, respectively, as shown in Figure 2d. Responsivity (R_λ) and EQE are important parameters to estimate the sensitivity of a device and can be calculated by the following equations:[39]

$$R_\lambda = (I_p - I_d)/P_\lambda S \quad (7)$$

$$EQE = R_\lambda hc/e\lambda \quad (8)$$

where I_p and I_d are photo current and dark current, P_λ and λ are incident power density and wavelength, h, c, and e are the Plank constant, velocity of light, and the charge of the electron, respectively. The effective exposure area, S, is estimated to be 0.0136 mm^2 for the device. As seen in Figure 2e,f, the maximum responsivity and EQE under 300 nm illumination at 5 V are calculated to be 18 A W^{-1} and 7.4×10^3%, respectively, indicating the good sensitivity of the SnO_2 MW-based PD. In particular, it is noteworthy that the UV/visible rejection ratio ($R_{300\ nm}/R_{400\ nm}$) is about 1.2×10^7 (Figure 2e), exceeding all the previously reported materials and devices (**Table 1** and Table S1, Supporting Information). The result demonstrates that the present SnO_2 MW-based PD possesses an excellent spectral selectivity of the visible-blind region, giving high potential for the application in the visible-blind sensors. Besides, the device shows 1.15 mA W^{-1} of responsivity at 0.01 V bias (inset of Figure 2e), indicating that it can work in a low energy consumption mode.

In addition, it is also expected that the PD should exhibit high sensitivity to weak signal which can be estimated by two important

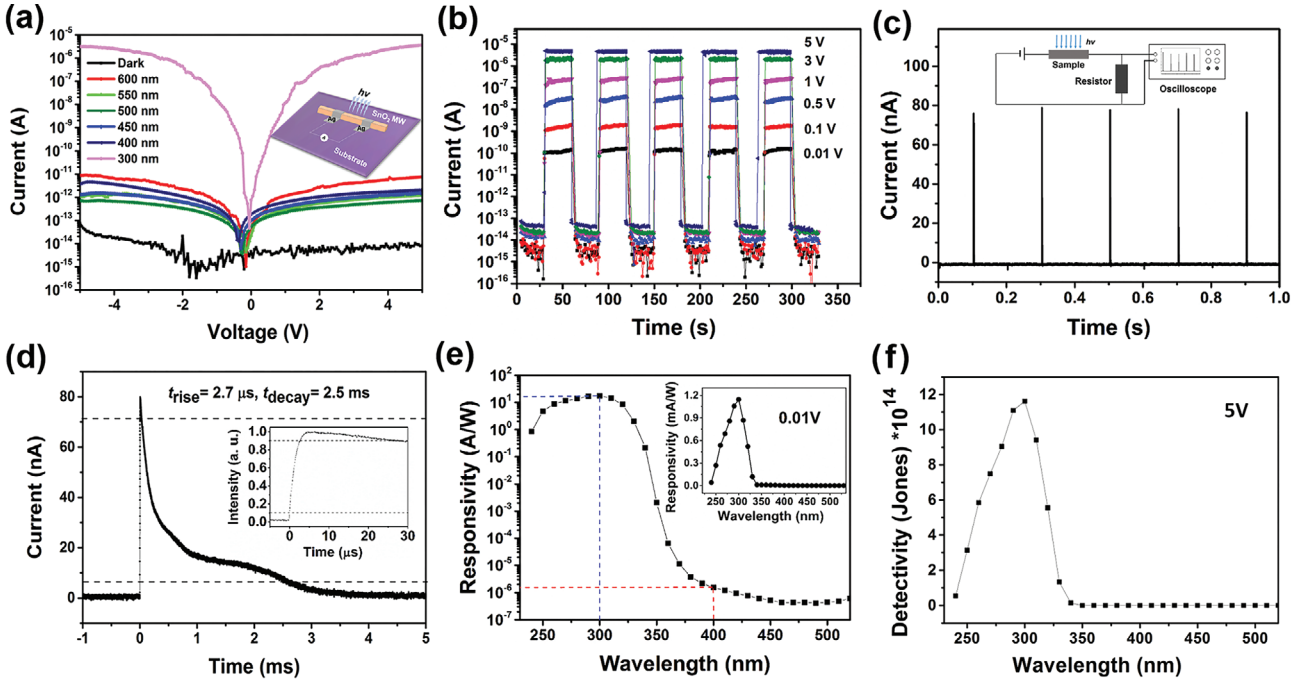

Figure 2. Photoresponse measurements of a single SnO_2 MW-based PD under ambient circumstance. a) *I–V* characteristics under dark and light illumination with different wavelengths (Inset: Schematic illustration of the single SnO_2 MW-based PDs). b) Time-dependent photo current measurements of the on–off behavior operated at voltages from 0.01 to 5 V under 300 nm light illumination. c) Transient current output to 10 Hz 355 nm laser pulse under 5 V bias (Inset: Schematic illustration of the measure circuit). d) Photo current rise and fall characteristics of a single pulse response from (c). (Inset: the enlarged part of the rise edge). e) Semi-log plot of the responsivity versus wavelength according to the spectral response measurement at 5 V (Inset: responsivity at 0.01 V). f) Linear plot of detectivity versus wavelength at 5 V.

parameters, that is, the D^* and the linear dynamic range (LDR). They can be calculated from the following equations:[14,47,48]

$$D^* = R_\lambda / \left(2eI_d/S\right)^{1/2} \tag{9}$$

$$\mathrm{LDR} = 20\log\left(I_p/I_d\right) \tag{10}$$

The D^* and the LDR are calculated to be 1.16×10^{15} cm $Hz^{1/2}$ W^{-1} (Jones) and 152 dB at 5 V under 300 nm light illumination (Figure 2f), which are even better than commercial Si and InGaAs PDs.[47]

Taking the advantages of the SnO_2 MWs, a p-CuI/n-SnO_2 heterojunction with superior photoelectric properties has also been configured (**Figure 3**a). Figure 3b–3d displays the photoelectric performances of the p-CuI/n-SnO_2 heterojunction-based PD. From the *I–V* characteristics in Figure 3b, it is noticed that the photo current of the device shows an asymmetry form under 300 nm light illumination. Additionally, the *I–t* curve shows a consistent, repeatable, and fast photoresponse feature at 0 V bias, as shown in Figure 3c. The results suggest the formation of p–n heterojunction at the interface of p-CuI and n-SnO_2, which induces the self-powered property and rectification effect.[14,18] According to the transient response

Table 1. Key parameters comparison of the p-CuI/n-SnO_2-based PD and others self-powered devices.

PDs	Wavelength [nm]	*I* (dark) [pA]	*I* (photo) [nA]	On/Off ratio	$R_{peak}/R_{400\ nm}$	Rise/Decay Time	R_λ [mA W^{-1}]	D^* (Jones)	Ref.
ZnO/Ga_2O_3	251	≈1	6	$\approx 6\times10^3$	6.9×10^2	0.1 ms/0.9 ms	9.7	6.9×10^{12}	[40]
ZnO/CuZnS	300	$\approx 8\times10^3$	30	3.7	–	0.5 μs/15 s	12	–	[41]
TiO_2/CuZnS	300	–	≈28	–	–	<0.2 s/<0.2 s	2.54	–	[42]
TiO_2/NiO	350	≈25	≈375	14	–	1.2 s/7.1 s	0.06	1.1×10^9	[43]
TiO_2/MeOTAD	410	–	≈100	–	–	0.12 s/0.06 s	10	–	[44]
TiO_2/PANI	320	≈300	$\approx 32\times10^{-2}$	≈1000	–	3.8 s/30.7 ms	3.6	3.9×10^{11}	[45]
ZnO/CuSCN	350	–	–	–	100	0.5 μs/6.7 μs	7.5	–	[46]
MgZnO/PANI	250	0.01	2.5	2.5×10^3	$\approx10^4$	<0.3 s/<0.3 s	0.16	1.5×10^{11}	[47]
SnO_2/CuZnS	300	0.1	1.8×10^{-2}	180	–	<45 μs/1.2 ms	1.6	5.4×10^{11}	[18]
SnO_2/CuI	300	≈0.01	≈1	$>10^5$	$>10^5$	0.3 ms/1.1 ms	8.98	1.98×10^{12}	This work

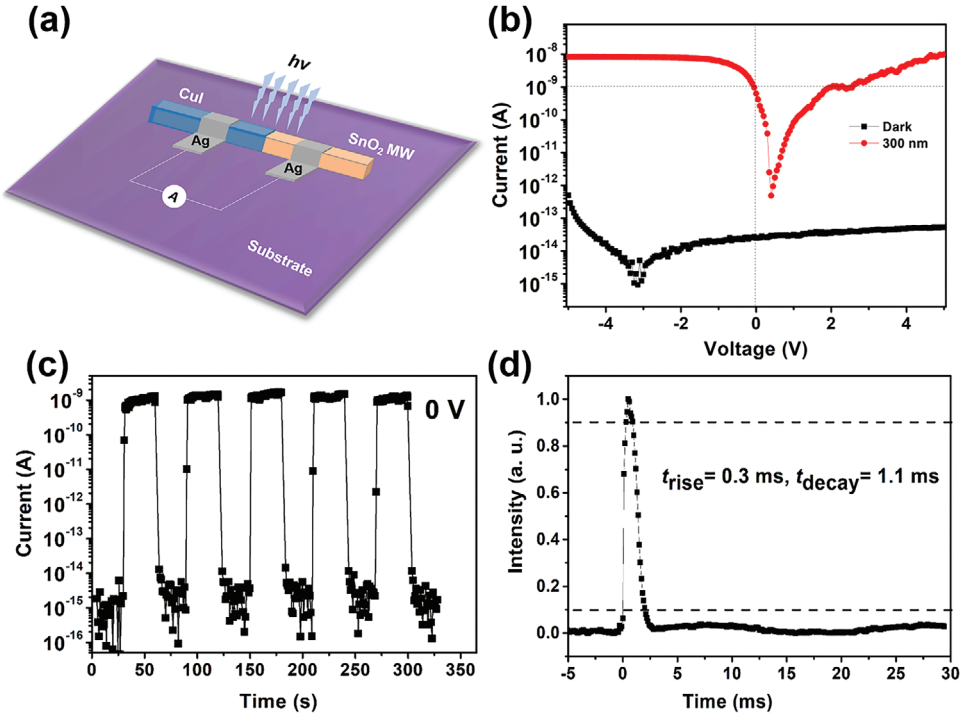

Figure 3. Photoelectric performances of the p-CuI/n-SnO_2 heterojunction-based PD measured under ambient circumstance. a) Schematic illustration of the p-CuI/n-SnO_2 microwire-based PD. b) *I–V* curves measured under dark and 300 nm light illumination. c) *I–t* curves measured at 0 V bias under 300 nm light illumination. d) Photo current rise and fall characteristics of a single pulse response of the transient current output to 10 Hz 355 nm laser pulse at 5 V bias.

of current output to 10 Hz 355 nm laser pulse under 5 V bias (Figure 3d and Figure S5a, Supporting Information), the rise and decay time of the device are estimated to be $t_{rise} \approx 0.3$ and $t_{decay} \approx 1.1$ ms, respectively. Furthermore, the p-CuI/n-SnO_2-based PD shows high photoelectric performances at 0 V bias, such as responsivity of 8.98 mA W^{-1}, specific detectivity of 1.98×10^{12} Jones and LDR of 106 dB, as shown in **Figure 4**a,b and Figure S5b, Supporting Information. The comparison of the photoelectric performances between the p-CuI/n-SnO_2-based PD and other self-powered devices are listed in Table 1.

The comparison of the responsivities between SnO_2 MW and the p-CuI/n-SnO_2-based PD under the light wavelengths from 600 to 240 nm at 5 and 0 V bias is shown in Figure S5c, Supporting Information, where the two curves show very similar increasing point of spectral response (≈350 nm) from the long wavelength. The CuI seems to not contribute to the photogenerated electron–hole pairs in the p-CuI/n-SnO_2-based device, although the calculated bandgap of CuI is ≈3.0 eV (≈413 nm) from absorption of UV light (Figure S5d, Supporting Information). To explain this phenomenon, *I–V* measurements have been performed and the results show that the CuI film did not show any response to UV light, as shown in Figure 4c. Consequently, a possible photoresponse mechanism for the self-powered p-CuI/n-SnO_2-based UV PD is proposed according to the energy-band diagram (Figure 4d), where the electron affinities (χ) are taken as 2.1 and 4.5 eV,[49,50] and the calculated bandgaps from UV–vis spectra of 3.0 and 3.6 eV are used for CuI and SnO_2, respectively. In Figure 4d, it is clear that a typical type-II heterojunction formed at the interface between CuI and SnO_2. When exposed to UV light illumination with energy higher than the bandgap of SnO_2, photoinduced electron–hole pairs are generated in SnO_2 and diffuse to the depletion region, then quickly separated by the built-in field, where electrons tend to move to the conduction band of SnO_2 while holes migrate to the valance band of CuI. Finally, the photo current generates and can be collected by the Ag electrodes at both ends at 0 V bias, thus it can work as an effective self-powered UV PD.

Besides, the realization of multifunctional detection using one device is also of significance to future sensors. The humidity sensing properties of the single SnO_2 MW-based device (the same device used in Figure 2) have been measured and the results are shown in **Figure 5**. It is observed that the static resistance of the SnO_2 MW decreases with the increase of relative humidity (RH) in air (Figure 5a). The resistance of the SnO_2 MW in dry air (DA, 6%) is calculated to be $\approx 8.3 \times 10^{12}$ Ω (as deduced from the dark current at 5 V), which is ≈350 times higher than that in 59% RH air (2.43×10^{10} Ω). It is obvious that water vapor in air has an important influence on the conductivity of the SnO_2 MW. The dynamic current response of the device under different RH circumstance has also been investigated and the results are displayed in Figure 5b. It can be seen that the current changes promptly when the sensor is switched to different RH. The response and recovery time (defined as the time spent to reach 90% of the final equilibrium value) are all less than 1 s (step limitation of the measurement system is 0.3 s). Besides, the responsivity (I_{RH}/I_{DA}) of the SnO_2 MW-based device presents a good linearity with RH in air (Figure 5c). The

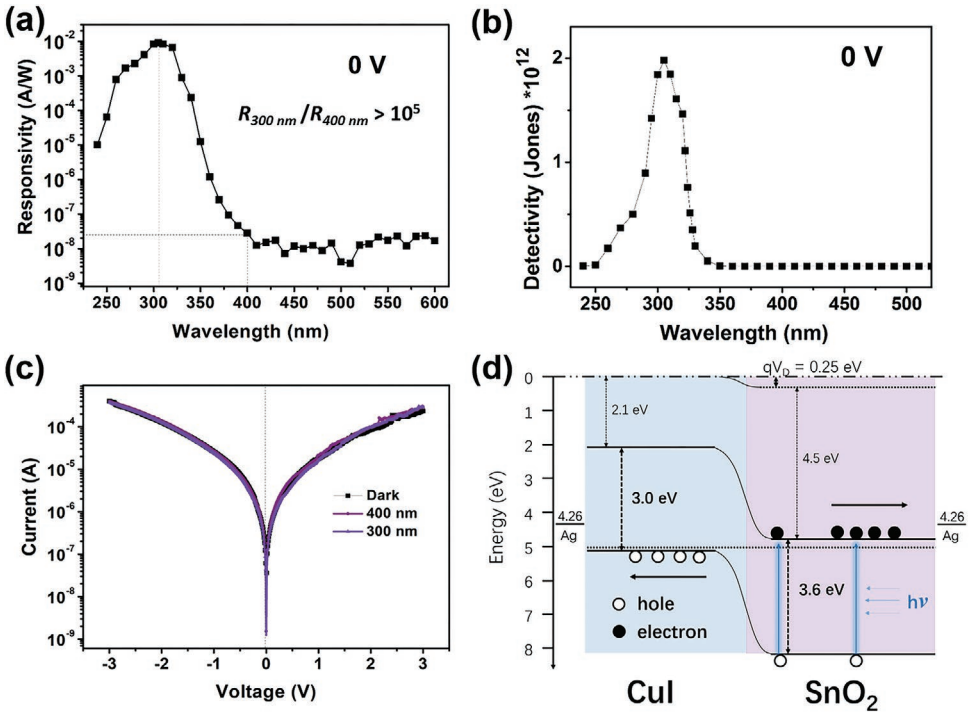

Figure 4. a) Plot of the responsivity versus wavelength according to the spectral response measurement of the p-CuI/n-SnO_2-based device at 0 V. b) Linear plot of detectivity versus wavelength at 0 V. c) *I–V* characteristics under dark, 400, and 300 nm light illumination of the CuI film, respectively. d) The energy-band diagram of the p-CuI/n-SnO_2-based device.

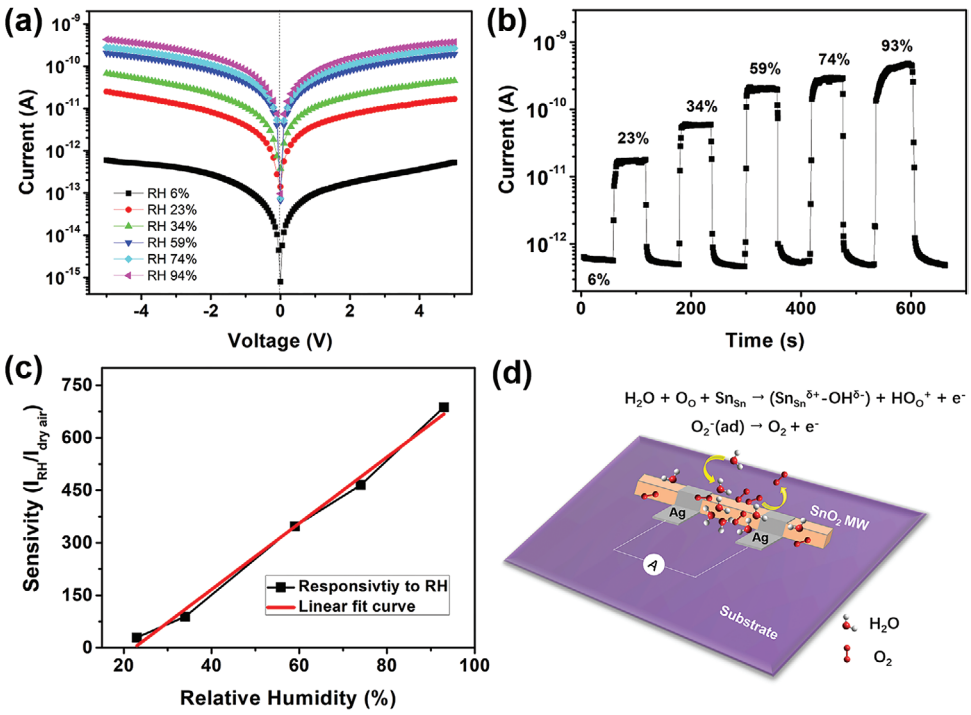

Figure 5. a) *I–V* curves and b) time response characteristics of the SnO_2 MW-based humidity sensor to dynamic switches between dry air (6%) and different RH (23–93%) at 25 °C and 5 V bias. c) Linear dependence of the relation between current response sensitivity and relative humidity. d) Schematic illustration of the mechanism of humidity sensing from low to high relative humidity for the SnO_2 MW-based device.

possible humidity sensing mechanism of the SnO_2 MW-based device is given in Figure 5d. For SnO_2, it is well known that the oxygen molecules can be adsorbed on the surface through reaction $O_2 + e^- \rightarrow O_2^-$ (ad) under low RH in air, which in turn results in a space charge region (or depletion layer) and a surface barrier that increases the resistance.[16,17] When the SnO_2 MW is exposed in a high RH environment, the pre-adsorbed oxygen on the surface can be displaced by competitive physisorption or chemisorption of water molecules. On the one hand, the dissociative adsorption of oxygen molecules release electrons to SnO_2 through reaction O_2^- (ad) $\rightarrow O_2 + e^-$.[16,17] On the other hand, the chemisorption of water molecules also provide electrons to SnO_2 via the dissociation of water which can be described in terms of Lewis acid–base reaction: $H_2O + O_O + Sn_{Sn} \rightarrow (Sn_{Sn}{}^{\delta+} - OH^{\delta-}) + HO_O{}^+ + e^-$.[51,52] Both chemisorption of water molecules and the dissociative adsorption of oxygen molecules processes enhance the concentration of electrons in the SnO_2 MW, leading to the decrease of resistance under a high RH environment.

3. Conclusion

In summary, highly crystallized SnO_2 MWs are synthesized by the CVD method. The SnO_2 MW-based UV PD shows an ultralow dark current ($\approx 10^{-13}$ A), ultrahigh on–off ratio ($>10^7$), UV/visible rejection ratio ($R_{300\ nm}/R_{400\ nm} > 10^7$), D^* (1.16×10^{15} Jones), LDR (152 dB), high responsivity (18 A W^{-1}), and fast photoresponse (t_{rise}/t_{decay} = 2.7 µs/2.5 ms) under 5 V. Furthermore, by taking the advantages of the superior properties of the SnO_2 MWs, a self-powered UV PD is realized based on the p-CuI/n-SnO_2 heterojunction, which shows an ultralow dark current ($\approx 10^{-14}$ A), ultrahigh on–off ratio ($>10^5$), UV/visible rejection ratio ($R_{300\ nm}/R_{400\ nm} > 10^5$), D^* (1.98×10^{12} Jones), LDR (106 dB), and responsivity (8.98 mA W^{-1}) at 0 V bias. Besides, the device also shows a fast and stable photoresponse with t_{rise} of 0.3 ms and t_{decay} of 1.1 ms. Additionally, the SnO_2 MWs show high and fast sensitivity to the ambient humidity change. Therefore, the SnO_2 MWs are promising semiconducting material for multifunctional applications in several fields such as photodetection and humidity sensing.

4. Experimental Section

Preparation of SnO_2 Microwires: All reagents and raw materials were used as received without any further treatment. SnO_2 MWs were synthesized by a simple CVD reaction method. Specifically, SnO_2 nanoparticles (Aladdin, 99.99%, metals basis, particle diameter 50–70 mm) and graphite powders (Aladdin, 99.95%, metals basis, 800 meshes) were mixed and ground with a weight ratio of 9:1, then the mixture were transferred to a 20 mL alumina boat which severed as the source, a piece of p-type Si substrate was placed above the source material of the alumina boat. The alumina boat was placed in the center of the temperature region in a horizontal tube furnace. During the growth process, the temperature of the furnace was ramped to 1300 °C at a rate of 15 °C per minute and maintained at 1300 °C for 80 min under a constant flow of argon 100 standard cubic centimeters (sccm) and oxygen of 2 sccm, respectively. After the furnace was cooled down to room temperature naturally, white straight freestanding MWs were formed both in the boat and on the surface of the substrate (Figure S1, Supporting Information).

Preparation of p-CuI/n-SnO_2: For the deposition of CuI, an individual SnO_2 MW was partially covered by a weigh paper and mounted on the plate of the vacuum thermal evaporator system. Commercial CuI (Aladdin, 99.5%, AR, 0.2 g) was used as the source and transferred on the molybdenum boat. During the growth, the plate was kept at 150 °C and the pressure in the system was controlled below 10^{-3} Pa, while the thickness of CuI was monitored by a film thickness gauge, the final thickness of CuI was ≈80 nm.

Characterizations of the Samples: The morphology, size and EDS analysis of as-prepared SnO_2 and p-CuI/n-SnO_2 MWs was investigated using a field-emission SEM (Zeiss Sigma). The crystal structure analysis was confirmed by a Bruker D8-A25 X-ray diffractometer using Cu Kα radiation (λ = 0.15406 nm) in the 2θ range from 15° to 70° using p-CuI/n-SnO_2 MWs and a single or multiple SnO_2 MWs. UV–vis absorption spectra were collected by measuring grounded powders of SnO_2 MW and CuI film which deposited on quartz substrate using a UV–vis spectrophotometer (Hitachi U-3900H). XPS test was carried out using a PHI 5300 ESCA system (Al Kα, 14 kV, 250 W).

Device Configuration and Measurement: SnO_2 MW and p-CuI/n-SnO_2 MW-based PDs were fabricated by a facile manually operate process. Specifically, SnO_2 MWs were carefully picked up by a tweezers and transferred onto a glass or SiO_2/Si substrate, two drops of Ag paste were manually patterned on the SnO_2 MW to serve as electrodes (inset image of Figure 2a). For the fabrication of p-CuI/n-SnO_2 MW-based PD, the process was the same except that one of the Ag pastes was patterned on CuI which covered on part of SnO_2 MW (Figure 3a). All the photoelectric measurements of MW-based PDs such as current–voltage (*I–V*) and the current–time (*I–t*) transient response characteristics were performed using a program-controlled semiconductor characterization system (Keithley 4200, USA) and four-probe station. A 450 W Xenon lamp equipped with a monochromator was utilized to provide light irradiation under different wavelengths. The light intensity was measured with a NOVA II power meter (OPHIR photonics). The spectral photo response was investigated from 240 to 600 nm. Furthermore, the instant photo response was evaluated by a system with a digital oscilloscope (Tektronix DPO5140B) and an Nd:YAG 355 nm pulsed laser system with 3–5 ns pulse duration. For the measurements of the SnO_2 MW-based device as a humidity sensor, *I–V* curves were obtained by putting the device into the spare space of different saturated salt solutions (LiBr, $MgCl_2 \cdot 6H_2O$, NaBr, NaCl, and K_2SO_4 which yielded 6%, 34%, 59%, 74%, and 93% RH, respectively, were used to act as humidity source) in air tight closed glass chambers at room temperature (25 °C). While *I–t* curves were obtained by alternative changing the humidity environment from LiBr to other saturated salt solutions.

Supporting Information

Supporting Information is available from the Wiley Online Library or from the author.

Acknowledgements

The authors would like to thank Siyuan Li, Dr. Yong Zhang, Dr. Wei Yang, and Dr. Hui Yang for discussions and experimental and technical assistance on humidity sensing. This work was supported by National Key R&D Program of China (No. 2017YFA0204600), National Natural Science Foundation of China (Nos. 12061131009 and 51872050), Science and Technology Commission of Shanghai Municipality (Nos. 21520712600 and 19520744300), the National Postdoctoral Science Foundation of China (2019M651362), the Foundation for PhD of Hubei Minzu University (MY2015B022), and the Natural Science Foundation of Science and Technology Department of Hubei Province (2020CFB698).

Conflict of Interest

The authors declare no conflict of interest.

Data Availability Statement

Research data are not shared.

Keywords

humidity sensors, self-powered, tin dioxide microwires, ultraviolet photodetectors

Received: July 12, 2021
Revised: July 28, 2021
Published online:

[1] S. Luo, J. Fan, W. Liu, M. Zhang, Z. Song, C. Lin, X. Wu, P. K. Chu, *Nanotechnology* **2006**, *17*, 1695.
[2] Ç. Kılıç, A. Zunger, *Phys. Rev. Lett.* **2002**, *88*, 095501.
[3] S. Das, V. Jayaraman, *Prog. Mater. Sci.* **2014**, *66*, 112.
[4] M. Batzill, U. Diebold, *Prog. Surf. Sci.* **2005**, *79*, 47.
[5] K. Ellmer, *Nat. Photonics* **2012**, *6*, 809.
[6] A. Kowal, M. Li, M. Shao, K. Sasaki, M. B. Vukmirovic, J. Zhang, N. S. Marinkovic, P. Liu, A. I. Frenkel, R. R. Adzic, *Nat. Mater.* **2009**, *8*, 325.
[7] M. Schreier, F. Héroguel, L. Steier, S. Ahmad, J. S. Luterbacher, M. T. Mayer, J. Luo, M. Grätzel, *Nat. Energy* **2017**, *2*, 17087.
[8] Q. Jiang, L. Zhang, H. Wang, X. Yang, J. Meng, H. Liu, Z. Yin, J. Wu, X. Zhang, J. You, *Nat. Energy* **2016**, *2*, 16177.
[9] D. Yang, R. Yang, K. Wang, C. Wu, X. Zhu, J. Feng, X. Ren, G. Fang, S. Priya, S. Liu, *Nat. Commun.* **2018**, *9*, 3239.
[10] J. Y. Huang, L. Zhong, C. M. Wang, J. P. Sullivan, W. Xu, L. Q. Zhang, S. X. Mao, N. S. Hudak, X. H. Liu, A. Subramanian, H. Fan, L. Qi, A. Kushima, J. Li, *Science* **2010**, *330*, 1515.
[11] G. Wen, L. Tan, X. Lan, H. Zhang, R. Hu, B. Yuan, J. Liu, M. Zhu, *Sci. China Mater.* **2021**, DOI: https://doi.org/10.1007/s40843-021-1665-1.
[12] X. S. Fang, J. Yan, L. F. Hu, H. Liu, P. S. Lee, *Adv. Funct. Mater.* **2012**, *22*, 1613.
[13] Y. Zhang, W. X. Xu, X. J. Xu, J. Cai, W. Yang, X. S. Fang, *J. Phys. Chem. Lett.* **2019**, *10*, 836.
[14] D. D. Hao, D. P. Liu, Y. K. Shen, Q. Q. Shi, J. Huang, *Adv. Funct. Mater.* **2021**, *31*, 2100773.
[15] D. Wang, F. Luo, M. Lu, X. Xie, L. Huang, W. Huang, *Small* **2019**, *15*, 1804404.
[16] L. F. Hu, J. Yan, M. Y. Liao, L. M. Wu, X. S. Fang, *Small* **2011**, *7*, 1012.
[17] L. Gan, M. Liao, H. Li, Y. Ma, T. Zhai, *J. Mater. Chem. C* **2015**, *3*, 8300.
[18] J. Cai, X. J. Xu, L. X. Su, W. Yang, H. Y. Chen, Y. Zhang, X. S. Fang, *Adv. Opt. Mater.* **2018**, *6*, 1800213.
[19] K. B. Sundaram, G. K. Bhagavat, *J. Phys. D: Appl. Phys.* **1983**, *16*, 69.
[20] H. Shi, B. Cheng, Q. Cai, X. Su, Y. Xiao, S. Lei, *J. Mater. Chem. C* **2016**, *4*, 8399.
[21] S. Park, S. W. Heo, W. Lee, D. Inoue, Z. Jiang, K. Yu, H. Jinno, D. Hashizume, M. Sekino, T. Yokota, K. Fukuda, K. Tajima, T. Someya, *Nature* **2018**, *561*, 516.
[22] J. Feldmann, N. Youngblood, M. Karpov, H. Gehring, X. Li, M. Stappers, M. L. Gallo, X. Fu, A. Lukashchuk, A. S. Raja, J. Liu, C. D. Wright, A. Sebastian, T. J. Kippenberg, W. H. P. Pernice, H. Bhaskaran, *Nature* **2021**, *589*, 52.
[23] H. Wu, Q. Dai, *Nature* **2021**, *589*, 25.
[24] V. Q. Le, T. H. Do, J. R. D. Retamal, P. W. Shao, Y. H. Lai, W. W. Wu, J. H. He, Y. L. Chueh, Y. H. Chu, *Nano Energy* **2019**, *56*, 322.
[25] Y. Ai, T. H. Hsu, D. C. Wu, L. Lee, J. H. Chen, Y. Z. Chen, S. C. Wu, C. Wu, Z. M. Wang, Y. L. Chueh, *J. Mater. Chem. C* **2018**, *6*, 5514.
[26] J. X. Chen, W. X. Ouyang, W. Yang, J. H. He, X. S. Fang, *Adv. Funct. Mater.* **2020**, *30*, 1909909.
[27] W. Yang, K. Hu, F. Teng, J. H. Weng, Y. Zhang, X. S. Fang, *Nano Lett.* **2018**, *18*, 4697.
[28] H. C. Fu, V. Ramalingam, H. Kim, C. H. Lin, X. S. Fang, H. N. Alshareef, J. H. He, *Adv. Energy Mater.* **2019**, *9*, 1900180.
[29] W. Yang, J. Chen, Y. Zhang, Y. Zhang, J. H. He, X. S. Fang, *Adv. Funct. Mater.* **2019**, *29*, 1808182.
[30] X. Xu, M. Tan, B. Corcoran, J. Wu, A. Boes, T. G. Nguyen, S. T. Chu, B. E. Little, D. G. Hicks, R. Morandotti, A. Mitchell, D. J. Moss, *Nature* **2021**, *589*, 44.
[31] Y. Wang, H. Wu, L. Xu, H. Zhang, Y. Yang, Z. L. Wang, *Sci. Adv.* **2020**, *6*, eabb9083.
[32] R. Q. Zhang, Y. Lifshitz, S. T. Lee, *Adv. Mater.* **2003**, *15*, 635.
[33] S. H. Sun, G. W. Meng, Y. W. Wang, T. Gao, M. G. Zhang, Y. T. Tian, X. S. Peng, L. D. Zhang, *Appl. Phys. A: Mater. Sci. Process.* **2003**, *76*, 287.
[34] B. Wang, Y. H. Yang, C. X. Wang, G. W. Yang, *J. Appl. Phys.* **2005**, *98*, 073520.
[35] C. Zheng, J. Wan, Y. A. O. Cheng, D. Gu, Y. Zhan, *Int. J. Mod. Phys. B* **2005**, *19*, 2811.
[36] J. Liu, X. Chen, W. Wang, B. Song, Q. Huang, *Cryst. Growth Des.* **2009**, *9*, 1757.
[37] Z. L. Li, M. K. Joshi, J. X. Chen, Z. M. Zhang, Z. Q. Li, X. S. Fang, *Adv. Funct. Mater.* **2020**, *30*, 2005291.
[38] Z. L. Li, F. Davar, J. X. Chen, Z. Q. Li, X. S. Fang, *ACS Appl. Nano Mater.* **2020**, *3*, 10190.
[39] H. Liu, N. Gao, M. Y. Liao, X. S. Fang, *Sci. Rep.* **2015**, *5*, 7716.
[40] B. Zhao, F. Wang, H. Y. Chen, L. X. Zheng, L. X. Su, D. X. Zhao, X. S. Fang, *Adv. Funct. Mater.* **2017**, *27*, 1700264.
[41] X. J. Xu, S. Shukla, Y. Liu, B. B. Yue, J. Bullock, L. X. Su, Y. M. Li, A. Javey, X. S. Fang, J. W. Ager, *Phys. Status Solidi RRL* **2018**, *12*, 1700381.
[42] X. J. Xu, J. X. Chen, S. Cai, Z. H. Long, Y. Zhang, L. X. Su, S. S. He, C. Q. Tang, P. Liu, H. S. Peng, X. S. Fang, *Adv. Mater.* **2018**, *30*, 1803165.
[43] L. X. Zheng, F. Teng, Z. M. Zhang, B. Zhao, X. S. Fang, *J. Mater. Chem. C* **2016**, *4*, 10032.
[44] Y. Xie, L. Wei, Q. Li, G. Wei, D. Wang, Y. Chen, J. Jiao, S. Yan, G. Liu, L. Mei, *Appl. Phys. Lett.* **2013**, *103*, 261109.
[45] L. X. Zheng, P. P. Yu, K. Hu, F. Teng, H. Y. Chen, X. S. Fang, *ACS Appl. Mater. Interfaces* **2016**, *8*, 33924.
[46] S. M. Hatch, J. Briscoe, S. Dunn, *Adv. Mater.* **2013**, *25*, 867.
[47] H. Y. Chen, P. P. Yu, Z. M. Zhang, F. Teng, K. Hu, X. S. Fang, *Small* **2016**, *12*, 5809.
[48] M. Y. Liao, *Funct. Diamond* **2021**, *1*, 29.
[49] S. Baek, D. Kwon, Y. C. Kim, J. Myoung, *ACS Appl. Mater. Interfaces* **2020**, *12*, 6037.
[50] Z. Zhang, C. Shao, X. Li, L. Zhang, H. Xue, C. Wang, Y. Liu, *J. Phys. Chem. C* **2010**, *114*, 7920.
[51] Q. Kuang, C. Lao, Z. L. Wang, Z. Xie, L. Zheng, *J. Am. Chem. Soc.* **2007**, *129*, 6070.
[52] H. Zhu, Q. Li, Y. Ren, Q. Gao, X. Xing, *Small* **2018**, *14*, 1703974.
[53] D. Zhang, Y. Cao, P. Li, J. Wu, X. Zong, *Sens. Actuators, B* **2018**, *265*, 529.

